




## Steady State Characteristics of the Terrestrial Geopauses

Huy-Sinh Trung<sup>1</sup> , Michael W. Liemohn<sup>2</sup> , and Raluca Ilie<sup>3</sup> 

<sup>1</sup>Department of Physics, University of Michigan, Ann Arbor, MI, USA, <sup>2</sup>Department of Climate and Space Sciences and Engineering, University of Michigan, Ann Arbor, MI, USA, <sup>3</sup>Department of Electrical and Computer Engineering, University of Illinois at Urbana-Champaign, Urbana, IL, USA

## Key Points:

- Four definitions of the geopause are compared: number density, mass density, plasma pressure, and last closed field line (magnetopause)
- Multifluid magnetohydrodynamic modeling is used to calculate these geopauses for idealized north and south interplanetary magnetic field
- The magnetopause is farthest out during north interplanetary field, but the plasma geopauses are farthest during south field

## Correspondence to:

H.-S. Trung,  
trunghs@umich.edu

## Citation:

Trung, H.-S., Liemohn, M. W., & Ilie, R. (2019). Steady state characteristics of the terrestrial geopauses. *Journal of Geophysical Research: Space Physics*, 124, 5070–5081. <https://doi.org/10.1029/2019JA026636>

Received 19 FEB 2019

Accepted 10 APR 2019

Accepted article online 23 MAY 2019

Published online 4 JUL 2019

**Abstract** The boundary separating solar wind plasma from ionospheric plasma is typically thought to be the magnetopause. A generalization of the magnetopause concept called the geopause was developed by Moore and Delcourt (1995, <https://doi.org/10.1029/95RG00872>). The geopause is a surface defined where solar wind quantities equal the ionospheric quantities. Geopause studies have helped characterize magnetospheric systems. However, comparative studies between the geopauses to the magnetopause have not been conducted. In this paper, we analyze the influence of inner boundary composition and interplanetary magnetic field (IMF) orientation on the steady state terrestrial geopauses and the magnetopause. This study simulates the Earth's magnetosphere by using the multifluid capabilities of the Block Adaptive Tree Solar wind Roe-type Upwind Scheme magnetohydrodynamics model within the Space Weather Modeling Framework. The simulations show that the dayside magnetopause was not influenced by the presence of oxygen in the outflow for both IMF orientations and was larger than the other geopauses. In contrast, the nightside magnetopause was sensitive to the conditions in the outflow. The nightside magnetopause was smaller than the other geopauses with southward IMF. With northward IMF, the nightside magnetopause was the largest structure in comparison with the plasma-based geopauses. Our results indicate that no single boundary surface dictates the transition from a solar wind dominated plasma to ionosphere dominated plasma.

## 1. Introduction

The first model of a boundary separating the solar wind plasma from the ionospheric plasma was developed by Chapman and Ferraro (1931). At this boundary, called the magnetopause, solar wind conditions dictate how well the solar wind interacts with the Earth's magnetosphere. During magnetic reconnection, the Dungey cycle describes how magnetic flux is transported from the dayside to the nightside magnetosphere (Dungey, 1961). The asymmetric reconnection rate is dependent on conditions in both the magnetospheric plasma and the solar wind (Cassak & Shay, 2007). The magnetospheric plasma sources include the solar wind and a nonnegligible ionospheric plasma.

Shelley et al. (1972) observed energetic fluxes of heavy ions in the inner magnetosphere exceeding proton fluxes in the kiloelectron volt range during a geomagnetic storm. Sharp et al. (1982) used International Sun-Earth Explorer 1 data collected in the plasma sheet to show that the ionosphere was a dominant source to the plasma sheet during active periods. Young et al. (1982) used 48 months of ESA-GEOS (Geostationary Earth Orbit Satellite) 1 data to demonstrate enhanced O<sup>+</sup> density in the magnetosphere during geomagnetic activity. Chappell et al. (1987) concluded that ionospheric outflows were large enough to account for observed magnetospheric plasma densities without the need for a solar wind.

With mounting evidence that the ionosphere was an important source of ions to the magnetosphere, Moore and Delcourt (1995) developed the concept of a geopause to help describe magnetospheric regions. The geopause is a surface defined by equal contributions of the solar wind to the ionospheric plasma. For example, the mass density geopause is the surface defined by the mass density of the solar wind equal to the mass density of the ionospheric plasma. The most well-known example of a geopause is the magnetopause.

However, the geopause is difficult to study directly with satellite data due to the presence of hydrogen ions in both the solar wind and the ionospheric plasma. Indirectly, Moore et al. (1999) used Polar data to show an increase in ionospheric plasma number density in response to a coronal mass ejection. This implied that the density geopause was displaced due to the coronal mass ejection compression. Chandler and Moore (2003)

also used Polar data to demonstrate the presence of plasmaspheric ions near the equatorial magnetopause region. This showed indirectly the presence of the dayside number density geopause. Fortunately, simulations circumvent this issue by tracking solar wind plasma and ionospheric plasma separately. Winglee (1998) used a numerical two-fluid magnetohydrodynamics (MHD) model to track solar wind hydrogen and ionospheric hydrogen. During northward IMF, the geopause was confined to the inner magnetosphere. During southward IMF, the geopause expanded into the nightside covering the near-Earth neutral line. The simulations showed that ionospheric plasma was an important source to the current sheet.

In reality, the ionospheric outflow is composed of not only hydrogen but also oxygen (Sharp et al., 1982; Shelley et al., 1972; Young et al., 1982) and possibly nitrogen (Ilie & Liemohn, 2016). Winglee (2000) corrected this issue by expanding the multifluid MHD (MF-MHD) model to include  $O^+$  along with the solar wind  $H^+$  and ionospheric  $H^+$  in the plasma. Winglee et al. (2002) used the same three-fluid model to quantitatively demonstrate that the mass loading of the ionospheric outflow diminished the cross polar cap potential by providing a momentum loss source term to the solar wind. Glocer et al. (2009), Wiltberger et al. (2010), and Ilie et al. (2013) have used MF-MHD (with only two fluids,  $H^+$  and  $O^+$ ) simulations to investigate the effects of ionospheric outflow from  $O^+$  on the magnetosphere. They also showed a reduction in the cross polar cap potential.

Xu et al. (2016) applied the concept of geopause to study composition boundaries at Mars. This study was the first time the concept of the “geopause” was quantitatively applied to another planet. They concluded that the magnetic lobes are dominated by ions from Mars. This implied that ion escape could occur not only at the plasma sheet but at the lobes.

So far, studies comparing the geopauses and magnetopauses have not been conducted. In fact, essentially missing in most of these studies is a direct comparison of the various definitions of geopause. While the structure and dynamics of the magnetopause are often discussed, the plasma geopauses defined by Moore and Delcourt (1995) have not been placed into context relative to the magnetopause. This study addresses this issue with a systematic numerical study of four different geopause definitions, using a MF-MHD model within a coupled modeling framework. This study focuses on the static configurations of these geopause locations rather their dynamics. We apply several different inner boundary condition specifications as well as two standard interplanetary magnetic field (IMF) cases, purely northward and purely southward.

## 2. Methods

We employ the Space Weather Modeling Framework (SWMF; Tóth et al., 2012) to simulate the magnetospheric system. The SWMF is a modular software framework capable of linking different models to simulate the system reliably and efficiently. It has been used to successfully model processes in Earth's magnetosphere, such as storm dynamics (Ilie et al., 2010a, 2010b, 2013; Meng et al., 2012, 2013; Tóth et al., 2007; Zhang et al., 2007), solar wind mass and energy coupling to the magnetosphere (Ilie et al., 2010a, 2010b, 2013; Ridley, 2007; Welling & Ridley, 2010; Yu & Ridley, 2009), and ionosphere coupling with the magnetosphere (Glocer et al., 2009; Ilie et al., 2015a, 2015b; Zhang et al., 2007). The SWMF has also been systematically validated through several community-wide “challenges” (Pulkkinen et al., 2010, 2011, 2013; Rastätter et al., 2011, 2013; Shim et al., 2012) and even monthlong simulations (Haiducek et al., 2017) and multiyear real-time nowcasting validation (Liemohn et al., 2018). Therefore, even though no data-model comparisons are made in this study, the results from the SWMF have been shown to be realistic, and therefore, the systematic trends to be highlighted below are robust. For this endeavor, the two systems coupled are the global magnetosphere and the ionosphere. The ionospheric electrostatic potential model used is the Ridley Ionosphere Model (RIM; Ridley & Liemohn, 2002; Ridley et al., 2004), which solves for the 2-D height integrated potential of the ionosphere. RIM passes information about the potential to the global magnetosphere model, while the global magnetosphere model provides field-aligned current information to RIM. RIM uses a conductance model that includes solar extreme ultraviolet, starlight, and polar cap conductance.

### 2.1. Global Magnetosphere Modeling

The magnetospheric plasma has a solar wind component and an ionospheric component. To capture the physics of a multicomponent plasma, we use MF-MHDs. Within the SWMF, the Block-Adaptive-Tree Solar wind Roe-type Upwind Scheme (Powell et al., 1999) models MF-MHD and enables the tracking of individual plasma pressures, mass densities, and velocities. For the simulations presented in this study, we use either a two- or a three-fluid plasma for our simulations. The solar wind plasma is always modeled using  $H^+$ .

**Table 1**  
*Inner Boundary Conditions*

Parameter Name	Case 1	Case 2	Case 3	Case 4
No. of fluids	2	2	3	3
	Solar wind H <sup>+</sup>	Solar wind H <sup>+</sup>	Solar wind H <sup>+</sup>	Solar wind H <sup>+</sup>
MHD fluids	Ionospheric H <sup>+</sup>	O <sup>+</sup>	Ionospheric H <sup>+</sup> O <sup>+</sup>	Ionospheric H <sup>+</sup> O <sup>+</sup>
Percentage composition by number	100% iono H <sup>+</sup>	100% O <sup>+</sup>	50 % iono H <sup>+</sup> 50% O <sup>+</sup>	94% iono H <sup>+</sup> 6% O <sup>+</sup>
Total number density (/cm <sup>3</sup> )	28	28	28	14.875
Total mass density (amu/cm <sup>3</sup> )	28	448	240	28
Ion temperature (10 <sup>4</sup> K)	2.5	2.5	2.5	2.5

The ionospheric plasma is modeled using either H<sup>+</sup> or O<sup>+</sup>, or both. A summary of the different plasma compositions used can be found in Table 1. For the runs where H<sup>+</sup> is present in both the ionospheric plasma and the solar wind plasma, H<sup>+</sup> is distinguished by its source. The equations of MF-MHD are

$$\frac{\partial \rho_s}{\partial t} + \nabla \cdot (\rho_s \mathbf{u}_s) = S_{\rho_s}, \quad (1)$$

$$\frac{\partial \rho_s \mathbf{u}_s}{\partial t} + \nabla \cdot (\rho_s \mathbf{u}_s \mathbf{u}_s + I p_s) = n_s q_s (\mathbf{u}_s - \mathbf{u}_+) \times \mathbf{B} + \frac{n_s q_s}{n_e} (\mathbf{J} \times \mathbf{B} - \nabla p_e) + S_{\rho_s \mathbf{u}_s}, \quad (2)$$

$$\frac{\partial p_s}{\partial t} + \nabla \cdot (p_s \mathbf{u}_s) = -(\gamma - 1) p_s \nabla \cdot \mathbf{u}_s + S_{p_s}, \quad (3)$$

$$\frac{\partial \mathbf{B}}{\partial t} - \nabla \times (\mathbf{u}_+ \times \mathbf{B}) = 0, \quad (4)$$

Equation (1) is the mass equation, equation (2) is the momentum equation, equation (3) is the pressure equation, and equation (4) is Faraday's law.  $\rho_s$ ,  $n_s$ ,  $\mathbf{u}_s$ ,  $q_s$ , and  $p_s$ , denote the mass density, number density, velocity, charge, and pressure of the ion species.  $n_e$  denotes the number density of the electron plasma.  $e$  is the elementary charge.  $p_e$  is the electron gas pressure. It is taken to be 0.2 times the total ion pressure (Glocer et al., 2009).  $I$  is the unit dyadic tensor.  $\gamma$  is the adiabatic index and takes the value of 5/3.  $\mathbf{u}_+$  is the all-species-averaged velocity defined as

$$\mathbf{u}_+ = \frac{\sum_s q_s n_s \mathbf{u}_s}{en_e}. \quad (5)$$

$S_{\rho_s}$ ,  $S_{\rho_s \mathbf{u}_s}$ , and  $S_{p_s}$  are the source terms for the mass, momentum, and pressure ion equations. For Earth magnetospheric simulations, the mass and pressure source terms are neglected. We assume a collisionless plasma and neglect mass and pressure source terms as well as chemical reactions. However, the momentum source term cannot be neglected. The two stream instability limits the relative velocity between ion fluids parallel to the magnetic field. This instability cannot be resolved directly with our grid resolution. We use the artificial friction source term introduced by Glocer et al. (2009) to keep the relative velocity between ion fluids to realistic values. The momentum source term takes the form

$$S_{\rho_s \mathbf{u}_s} = \frac{1}{\tau_c} \sum_{i \neq s} \min(\rho_s, \rho_i) (\mathbf{u}_i - \mathbf{u}_s) \left( \frac{|\mathbf{u}_s - \mathbf{u}_i|}{u_c} \right)^{\alpha_c}. \quad (6)$$

$\tau_c$ , the cutoff time scale, is set to 1,000 s.  $u_c$ , the cutoff velocity, is set to 100 km/s.  $\alpha_c$ , the cutoff exponent, is set to 2.  $i$  is the index denoting the other ion fluids.

For more details on the derivation of the MF-MHD equations see Glocer et al. (2009). The coordinate system used is Geocentric Solar Magnetospheric. The simulation domain is  $(X, Y, Z) = [-224, 32] \times [-128, 128] \times [-128, 128]$ . The simulation time is set to 12 hr. Due to the idealized nature of this study, the Earth's rotation axis and magnetic dipole are aligned along the  $Z$  axis.

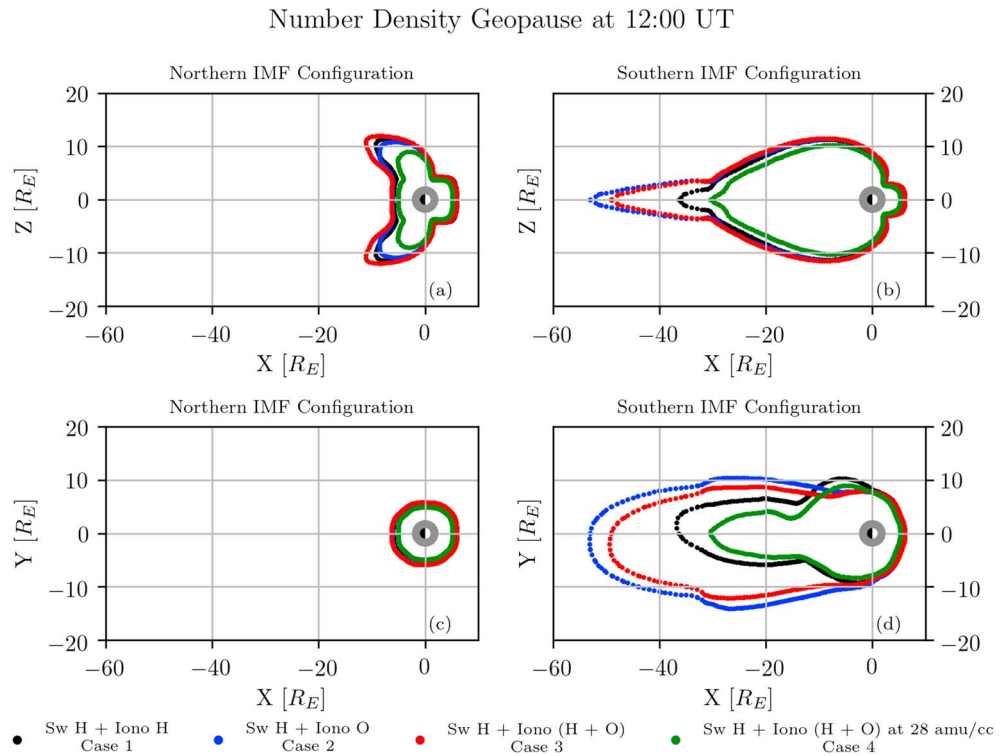


**Figure 1.** Number density geopause. (a) Meridional cut for northward IMF. (b) Meridional cut for southward IMF. (c) Equatorial cut for northward IMF. (d) Equatorial cut for southward IMF. IMF = interplanetary magnetic field.

### 2.1.1. Outer Boundary Conditions

The solar wind is introduced at the outer boundary of the system ( $X = 32 R_E$ ). For the simulations presented in this study, we use two types of solar wind magnetic field conditions. For all runs, the solar wind velocity, magnetic field intensity, mass density, and temperature are constant. The velocity of the solar wind is only in the  $X$  direction with a value of  $-450$  km/s. The mass density of the solar wind is  $8.7$  amu/cm<sup>3</sup>. The temperature is set to  $1.2 \times 10^5$  K. The magnetic field polarity is reversed at a set time. In the south-to-north IMF case, the solar wind has its IMF  $B_z$  component of  $+10$  nT and at 8:00 UT, the solar wind reverses to  $-10$  nT and the simulation continues for 4 hr. In the north-to-south case, the solar wind has its IMF  $B_z$  component set to  $-10$  nT for the first 4 hr of the simulation; then at 4:00 UT, the solar wind's IMF reverses to  $+10$  nT for the next 8 hr. This solar wind configuration studied is the same as that used by previous studies (Liemohn & Welling, 2016; Welling & Ridley, 2010). Note that only the results at the end of the 12-hr simulation will be shown and discussed below. That is, this study focuses on the static structure of the various geopause locations, rather than the dynamics of these boundaries (that will be the focus of a follow-on study).

### 2.1.2. Inner Boundary Conditions

The inner boundary is the source of ionospheric plasma in our simulations. It is a diffusive boundary set at a geocentric radius of  $2.5 R_E$ . For this study, we treat four different inner boundary conditions corresponding to different ionospheric plasma compositions. The inner boundary conditions are presented in Table 1.

Welling and Liemohn (2014) have discussed the use of steady state boundary conditions in numerical simulations. Specifically, they examined the use of an inner boundary density specification with no assigned outflow velocity, allowing the forces within the MHD model to drive the outflow. While these types of outflows are not physically self-consistent, they can reproduce large-scale structures.

## 3. Results

We present meridional ( $X$ - $Z$  plane,  $Y = 0$ ) and equatorial ( $X$ - $Y$  plane,  $Z = 0$ ) cuts of the geopause at 12:00 UT. To determine the geopause location, we cycle through each cell, calculating the ratio of the solar wind quantity to the total plasma quantity at the cell vertices. The cells must encapsulate the value 0.5, the

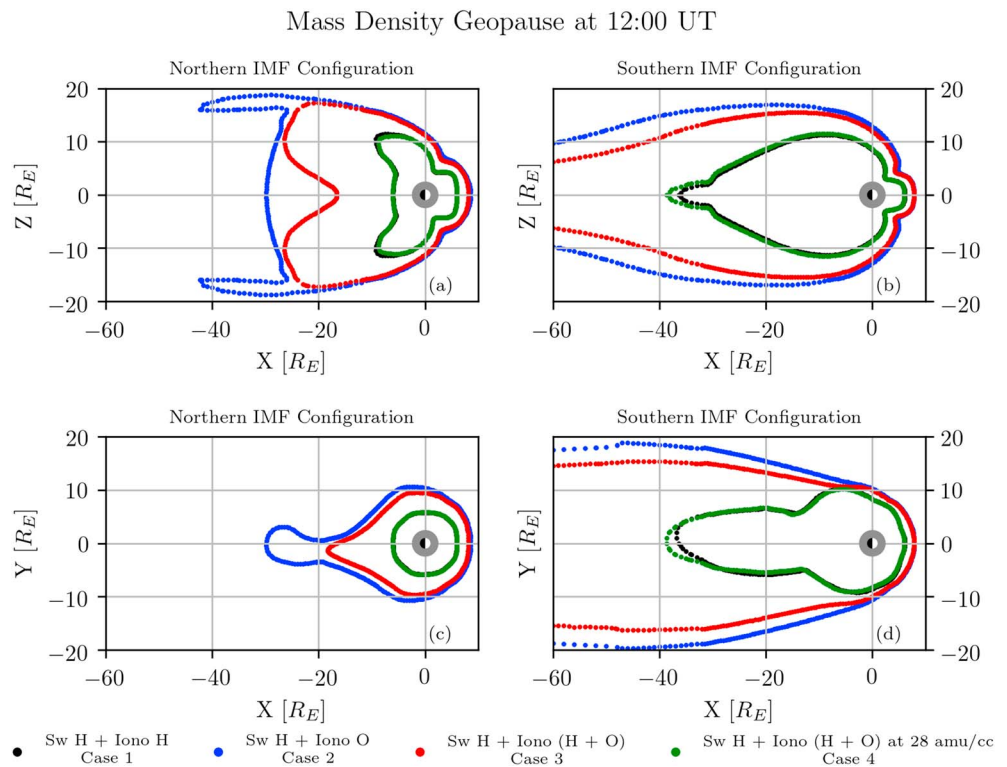


**Figure 2.** Mass density geopause. (a) Meridional cut for northward IMF. (b) Meridional cut for southward IMF. (c) Equatorial cut for northward IMF. (d) Equatorial cut for southward IMF. IMF = interplanetary magnetic field.

ratio at which the contributions from the solar wind and the ionospheric plasmas are equal. Then, we perform a linear interpolation along the cell edges to mark the coordinates of the geopause. The magnetopause is defined by the last closed magnetic field line (Siscoe et al., 2001; Song et al., 1999). It is found by drawing iteratively field lines along the Sun-Earth line. The definition of the magnetopause used in this paper differs from the classical definition which relies on identifying regions in the magnetosphere with large currents. Identification of the magnetopause using the classical definition is unreliable in cases where the incoming solar wind is northward.

### 3.1. Geopause Comparisons From Outflow

Figure 1 shows the number density geopause for the different IMF configurations at 12:00 UT. For northward IMF (Figures 1a and 1c), the number density geopauses across all outflow conditions are similar. In the meridional plane, the geopauses have a lobe structure. In the southward IMF case (Figures 1b and 1d), the number density geopause projections in the meridional and equatorial plane have a larger cross-sectional area with increasing oxygen content at the inner boundary for the cases with identical number densities (black, red, and blue lines). When comparing the inner boundaries with equal mass densities (green and black lines), the number density geopause has a larger projected area with the inner boundary with a higher particle content.

The mass density geopauses are displayed in Figure 2. The northward IMF cases (Figures 2a and 2c) show an ordering by the mass density of the ionospheric outflow. In the dayside, the outflows with significant portions of oxygen ions (blue and red lines) have a structure that is  $\sim 2 R_E$  further sunward of the lighter outflow cases. In the nightside, the mass density geopauses extend more antisunward, with increasing mass densities at the inner boundary. Unlike the equatorial number density geopauses, the equatorial mass density geopauses do not share the same structure. The equatorial mass densities display an asymmetry across the  $X$  axis. This asymmetry grows with increasing oxygen content at the inner boundary. The southward IMF cases (Figures 2b and 2d) have a projected surface area in the meridional and equatorial plane that increases with respect to the mass density at the inner boundary. Similar to the northward IMF case, the dayside mass density geopause is further along the Sun-Earth line with increasing oxygen content in the outflow.



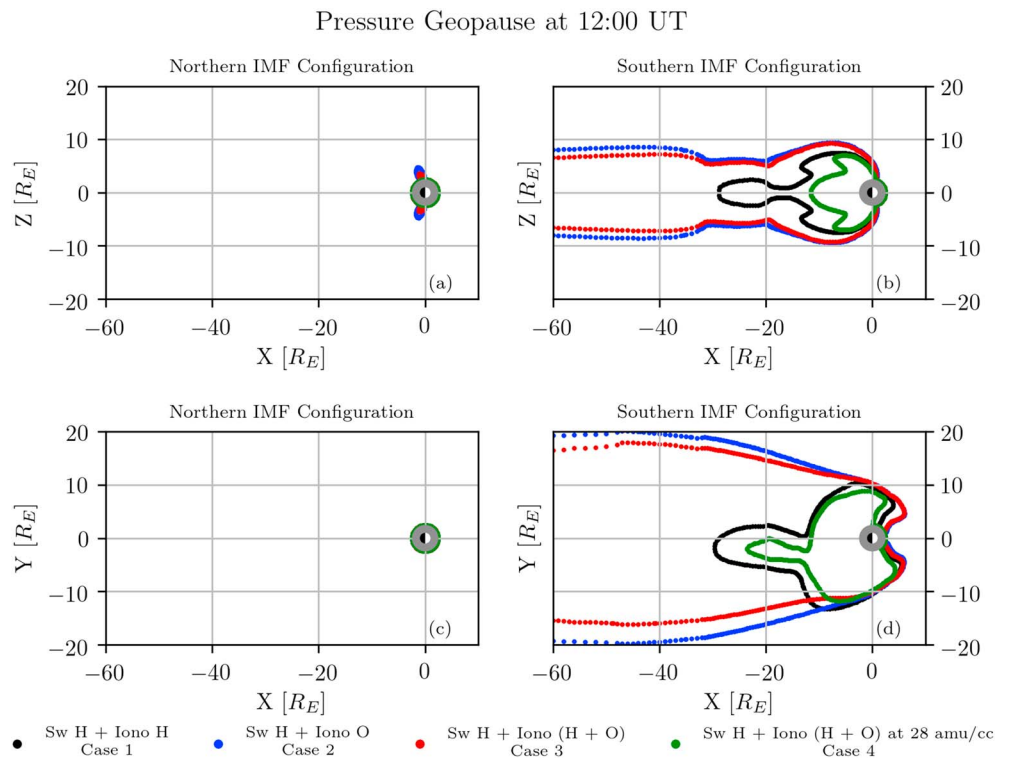


**Figure 3.** Pressure geopause. (a) Meridional cut for northward IMF. (b) Meridional cut for southward IMF. (c) Equatorial cut for northward IMF. (d) Equatorial cut for southward IMF. IMF = interplanetary magnetic field.

Figure 3 shows the pressure geopause locations for the four outflow cases. The pressure geopauses for northward IMF (Figures 3a and 3c) are not very extensive. In the meridional plane, there is a very small lobe structure associated with the outflows with oxygen (red and blue lines). In the equatorial plane, the pressure geopauses are at the simulation inner boundary. In the southward IMF case (Figures 3b and 3d), the pressure geopause size increases with increasing inner boundary mass density. The two cases with mostly  $O^+$  outflow have extremely long pressure geopause tails, extending past the end of the plot at  $-60 R_E$  and, in fact, going to  $\sim -145 R_E$  for the 50:50 hydrogen-oxygen mix at the inner boundary and to  $\sim -165 R_E$  downstream of Earth for the pure oxygen inner boundary. Note, however, that the pressure geopause does not

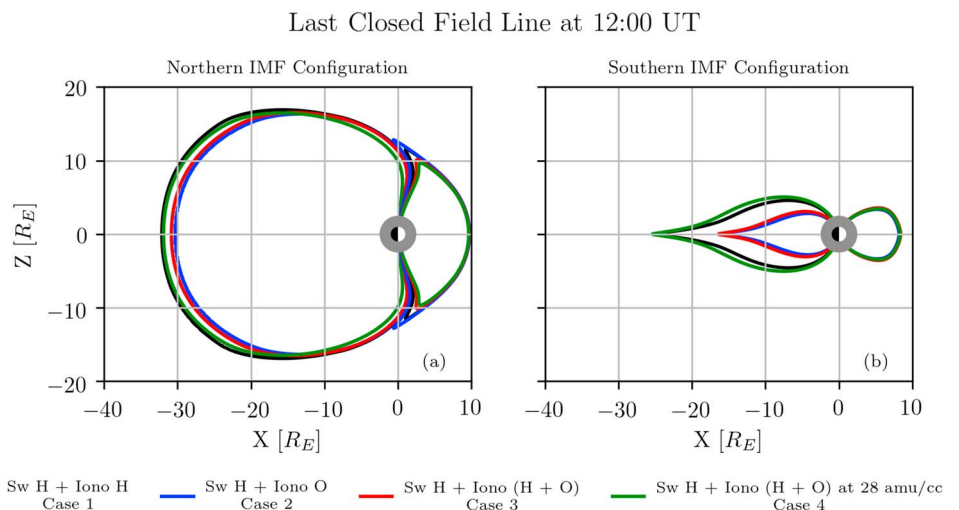


**Figure 4.** (a) Magnetopause projection in the meridional plane when the IMF is northward. (b) Magnetopause projection in the meridional plane when the IMF is southward. IMF = interplanetary magnetic field.

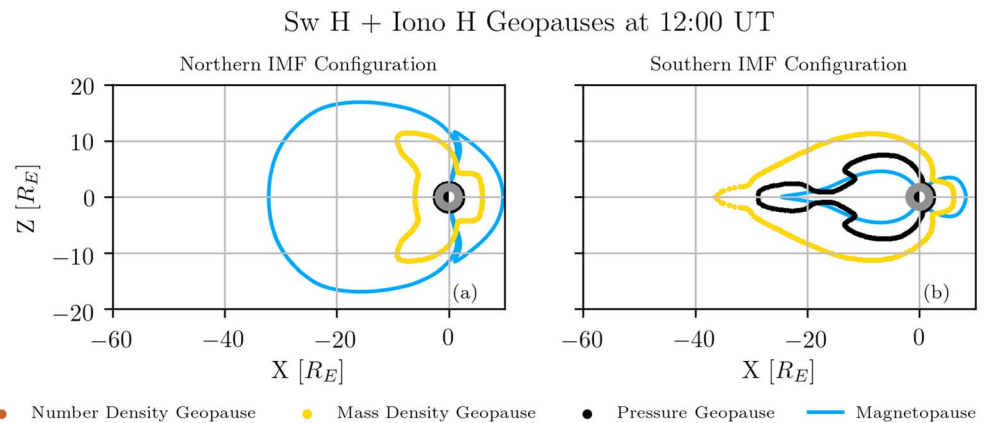


**Figure 5.** Geopauses for a plasma composed of solar wind and ionospheric hydrogen in the meridional plane. (a) Northward IMF. (b) Southward IMF. Note that the mass density geopause and the number density geopause are identical. IMF = interplanetary magnetic field.

extend into the dayside equatorial magnetosphere. For both northward and southward IMF, this is a region for which the plasma pressure is dominated by solar wind origin particles.

For comparison, let us now consider the last closed field line for the four boundary density cases and IMF settings. The magnetopause structures of the different outflow cases are very similar for northward IMF (Figure 4a). In the dayside, the magnetopauses overlap along the Sun-Earth line. In the nightside, the magnetopauses of the heavier outflow cases are  $\sim 2 R_E$  closer to Earth than the lighter cases. Similar to the northward IMF case, the dayside magnetopause for the southward IMF case is nearly the same for all types of outflow used in this study (Figure 4b). However, the nightside magnetopause structure is larger for the lighter outflow cases (green and black lines) than the heavier outflow cases (red and blue lines). The magnetopause formed by the lighter cases are separated by  $\sim 10 R_E$  from the heavier cases.

### 3.2. Comparisons Between the Geopauses and Last Closed Field Line

In the previous subsection, we have analyzed the influence of inner boundary conditions on the individual geopause definitions. Now, we are comparing the four geopauses for a given inner boundary case.

Figure 5 presents the four geopause boundaries for Case 1 (solar wind  $H^+$  and ionospheric  $H^+$ ), with only ionospheric  $H^+$  set at the inner simulation boundary. For this case, the outflowing particles are all protons, so the number density of the ionospheric origin plasma is identical to its mass density. Therefore, these two geopauses are identical and only the mass density curve is visible in the plots. In the northward IMF case, the magnetopause extends the farthest out from the planet, with the density geopauses next and the pressure geopause at the simulation inner boundary. The ordering is completely different for the southward IMF

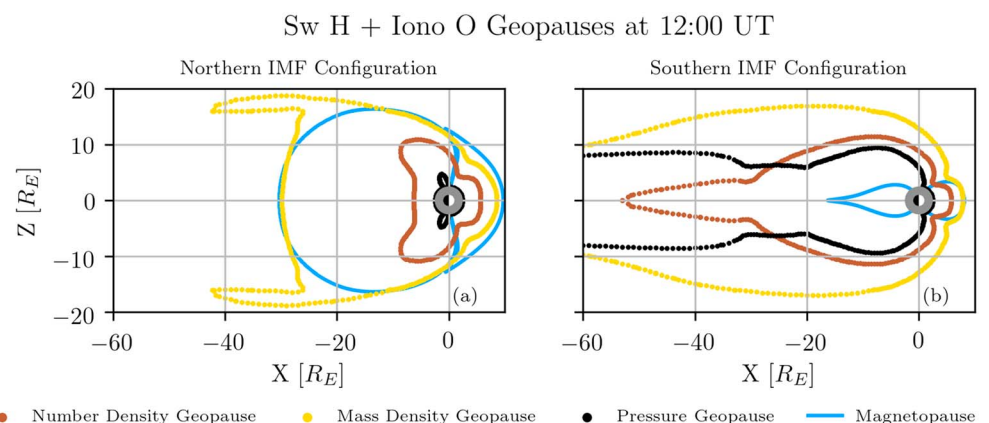


**Figure 6.** Geopauses for a plasma composed of solar wind hydrogen and ionospheric oxygen in the meridional plane. (a) Northward IMF. (b) Southward IMF. IMF = interplanetary magnetic field.

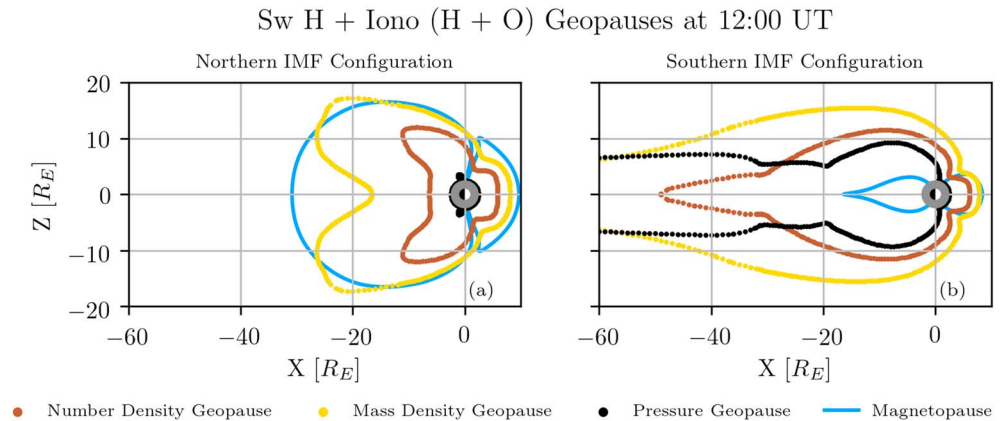


**Figure 7.** Geopauses for a plasma composed of solar wind hydrogen, ionospheric hydrogen and oxygen in the meridional plane. (a) Northward IMF. (b) Southward IMF. IMF = interplanetary magnetic field.

case, especially on the nightside, where the density geopauses extend the farthest, followed by the pressure geopause, and finally the last closed field line closest to the Earth. On the dayside, the magnetopause still extends the farthest, just beyond the density geopause.

At the other extreme outflow case where  $O^+$  is the sole ionospheric species (Case 2), Figure 6 displays the four geopause boundaries. For northward IMF, the shape and size of the magnetopause and number density geopause are similar to Case 1. The pressure geopause is still confined to the inner boundary but has a very small lobe structure. On the nightside, the mass density geopause is the largest structure. The ordering by extent along the Sun-Earth line is mass density geopause, magnetopause, number density geopause, and pressure geopause. In contrast for the dayside, the magnetopause is the largest, followed by the mass density geopause, number density geopause, then the pressure geopause. For southward IMF, the ordering for longest reach in the nightside is the pressure geopause, the mass density geopause, the number density geopause, and the magnetopause. At the dayside, the ordering is still the same as it was for northward IMF, magnetopause, mass density geopause, number density geopause, and pressure geopause.

For a 50:50  $H^+$  to  $O^+$  outflow composition (Case 3), the composition boundaries show an intermediate picture for the mass density geopause in northward IMF (Figure 7). That is, the size and shape of the mass density geopause are between both Case 1 and Case 2. The pressure geopause has a smaller lobe structure compared to Case 2. In the nightside, the geopause structure reaching the farthest is the magnetopause, followed by the mass density geopause, number density geopause, and pressure geopause. In the dayside, the ordering by largest extent is the magnetopause, mass density geopause, number density geopause, and the pressure geopause. For southward IMF, the geopause ordering structure by largest extent is the pressure geopause, mass density geopause, number density geopause, and magnetopause. For northward IMF, in this case the ordering by largest extent is magnetopause, mass density geopause, number density geopause, and pressure geopause.

Figure 8 plots the four boundaries for both IMF configurations. For northward IMF, the magnetopause is once again the most dominant in the dayside and nightside structure, followed by the mass density geopause, number density geopause, and pressure geopause. For southward IMF, the nightside structure most dominant is the mass density geopause followed by the number density geopause, magnetopause, and pressure geopause. The dayside structure most dominant is the magnetopause, then the mass density geopause, number density geopause, and pressure geopause.

For northward IMF, the most dominant boundary in size is the magnetopause (Figures 5a, 6a, 7a, and 8a) with the number density and pressure geopauses that are confined close to Earth. However, the outflows with significant amounts of oxygen have a mass density geopause structure comparable in size to the magnetopause. For southward IMF, while the magnetopause dominates the dayside (Figure 5a, 6a, 7a, 8a), the other geopauses are much larger in cross-sectional area in the nightside with increasing outflow mass density.



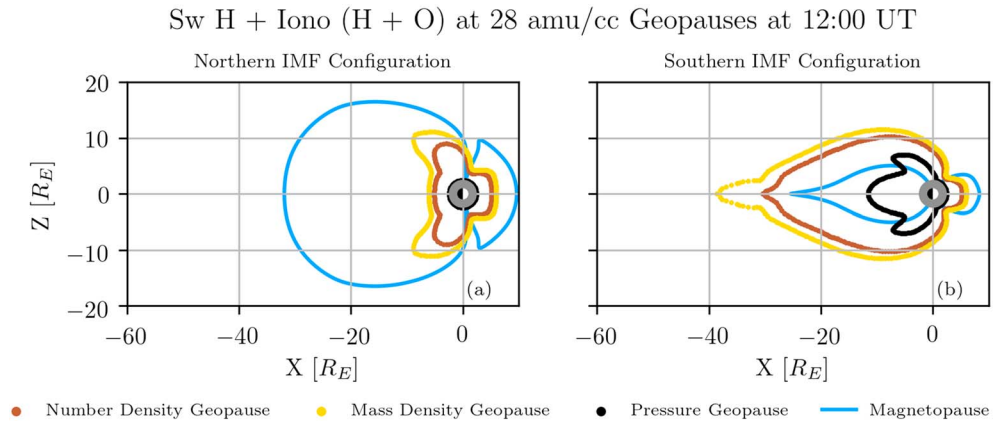


**Figure 8.** Geopauses for a plasma composed of solar wind hydrogen, ionospheric hydrogen, and oxygen in the meridional plane for an inner boundary mass density of 28 amu/cm<sup>3</sup>. (a) Northward IMF. (b) Southward IMF.

#### 4. Discussion

This study shows that the region of dominance by Earth-origin plasma or magnetic field can be significantly different depending on both the composition of the outflowing ions and the direction of the IMF. These differences in geopause extent matter because of how these parameters (number density, mass density, plasma pressure, and magnetic field) influence the physics of forces and flows in near-Earth space. In particular, these parameters appear in specific places within the MHD equations. Let us consider how each of the four parameters appears in equations (1) through (6) above. Number density,  $n_s$ , appears twice in the momentum equation as well as in the species-averaged velocity,  $\mathbf{u}_+$ . This means that number density plays a critical role in the magnetic induction equation. Mass density,  $\rho_s$ , appears not only throughout the continuity equation but also in the momentum equation and as a multiplier in the momentum source term. Its key role in  $S_{\rho_s \mathbf{u}_s}$  means that it modulates friction between the species. Plasma pressure,  $p_s$ , is ubiquitous in the pressure equation, of course, and also appears in the momentum equation through the electron pressure,  $p_e$  ( $p_e = 0.2 \sum_s p_s$ ). Furthermore, it combines with magnetic energy for conservation of energy calculations, therefore influencing energy transport. Finally, magnetic field,  $B$ , appears not only twice in the induction equation but also twice in the momentum equation, taking part in the flow of plasma through the system. In summary, it is seen that each term in the MHD equations is influenced by one or more of the parameters we have examined in our geopause results presented above.

Determining which geopause is the most important depends on the magnitudes of these terms within the MHD equations. We will not go into a detailed examination of this here because this study focused on idealized simulations. It is left to a later study to consider real-event intervals and the importance of a particular geopause location relative to another. One conclusion that can be drawn for now, however, is that there is no single surface in near-Earth space at which the physics switches from being governed by the Sun to being governed by the Earth. The differences in the geopauses presented above reveal that there is a transition from solar to Earth dominance in the physics of geospace. The magnetopause, often considered the outer boundary of Earth's influence in the solar system, is just one such boundary delineating a switch in Sun-Earth dominance of the physics. For northward IMF, this boundary is typically the farthest from the Earth, but for southward IMF, this boundary is typically the closest to the Earth.

Now let us consider the physics governing the shape of the boundaries. Within the momentum equation, a multiplier factor,  $n_s q_s / (n_e e)$ , is attached to the  $\mathbf{J} \times \mathbf{B}$  and  $\nabla p_e$  terms. For the simulations, this multiplier factor is simplified to  $n_s / n_e$ . Due to quasineutrality, the electron number density is equal to the total magnetospheric plasma number density. By applying the momentum equation to the solar wind, the multiplier factor at values of 0.5 becomes the density geopause. The shape and size of the density geopause are sensitive to the difference between the  $\mathbf{J} \times \mathbf{B}$  and  $\nabla p_e$ . During southward IMF, the gradient of the electron pressure increases at high latitudes due to the increased convection associated with the ionospheric species. This in turn causes the density geopause to be pushed out in the nightside and expand. In the dayside, the density geopause reduces in size due to the increased solar wind access through magnetic reconnection. For northward IMF, the reduction in magnetic convection will cause a greater influence from the solar wind in the

nightside magnetosphere. This results in the number density geopause to shrink in size. Since the mass density and pressure of the plasma species are related to the number densities of the plasma species, the mass density and pressure geopauses display similar behavior compared to the number density geopause. That is, the geopauses reduce in size during northward IMF and increase in size during southward IMF.

During northward IMF, the magnetopause responds poorly to the inner boundary mass density. This can be attributed to the lack of magnetic flux transport due to reconnection from the dayside to the nightside. The nightside differences in the magnetopause are due to high-latitude reconnection. During southward IMF, the dayside magnetopause locations between the different outflows are nearly identical. The different number density geopauses and pressure geopauses show that the solar wind dominates the magnetopause. Thus, ionospheric plasma plays a small part in dayside magnetic reconnection. Unlike the dayside magnetopause, the nightside magnetopause has shown some sensitivity to the composition of the inner boundary. Since the nightside magnetopause is contained within the number density geopause, the ionospheric plasma takes a greater part in the reconnection process compared to the dayside. For both IMF configurations, the confinement of the dayside pressure geopause to the inner boundary indicates the inability of MHD forces to enable outflow of ionospheric ions at lower latitudes. One explanation might be because of the lack of a causal outflow model. The other explanation is due to the absence of an inner magnetosphere model that includes drift physics.

Our simulations have not included a ring current model. Simulations that coupled ring current models to global MHD models have shown an increase in pressure by an order of magnitude at the inner magnetosphere compared to pure magnetospheric MHD runs (De Zeeuw et al., 2004; Gloer et al., 2013; Pembroke et al., 2012; Welling et al., 2018). Including an inner magnetosphere model will push the dayside pressure geopause further out of the inner boundary. However, the ring current models currently available in the SWMF do not distinguish the hydrogen plasma by its solar wind and ionospheric sources. This issue will be addressed in a future study by coupling BATS-R-US to the Hot Electron Ion Drift Integrator ring current model (Ilie et al., 2012). With the coupling of Hot Electron Ion Drift Integrator, we expect an expansion in size of the pressure geopause. One unanswered question relating to this study is, Where do the gyration, body forces, and friction terms in the momentum equations become prominent? This issue will be addressed in a future study analyzing the contribution of each term in the simulation region.

## 5. Summary and Conclusions

We have performed MF-MHD simulations where the ionospheric plasma was distinguished from the solar wind plasma. In these simulations, we used a passive inner boundary in which we maintained the same number density and varied the amount of oxygen. For the sake of comparison, we also used an inner boundary composition with oxygen with mass densities similar to a solely hydrogen plasma. We used two different solar wind conditions where the solar wind mass density, velocity, temperature, and magnetic field intensity were the same, but the polarities were different.

Our results indicate that the geopause structures formed during steady state were dependent on the abundance of oxygen ions in the ionospheric outflow during southward IMF. For northward IMF, only the mass density geopause varied with the inner boundary conditions. For the magnetopause in both IMF configurations, the dayside magnetopause did not vary between the different simulated ionospheric outflow cases. However, the nightside magnetopause was sensitive to the presence of oxygen ions present in the ionospheric outflow. In the north IMF case, a significant presence of oxygen in the outflow brings the nightside magnetopause further in along the Sun-Earth line by a few Earth radii compared to the oxygen-poor outflow cases. In the south IMF case, the nightside magnetopause along the Sun-Earth line is about 10 Earth radii further in for the oxygen-rich outflow simulations, compared to the oxygen-poor outflow simulations.

Within each set of simulations, we have seen that for northward IMF, the magnetopause was the largest structure in both the dayside and the nightside. This indicates that the solar wind dominated the magnetopause. For southward IMF, while the magnetopause still is the largest structure in the dayside, the geopauses in the nightside are comparable if not larger than the magnetopause. This indicates that ionospheric plasma can dominate in regions outside of the nightside magnetopause.

We have discussed the ramifications of the differences in these geopause locations which imply that the physics governing near-Earth space does not have a single surface at which the governing processes switch

from solar wind dominance to ionospheric dominance. Instead, there is a gradual transition as a set of physical processes associated with each parameter (number density, mass density, plasma pressure, and magnetic field) switch at different surfaces. The location of these surfaces strongly depends on both of the controlling factors considered in this study: the composition of the outflowing particles and the orientation of the IMF.

### Acknowledgments

This work was supported by NASA under grants 80NSSC17K0015 and NNX17AB87G. Trung was also supported by a NASA Earth and Space Science Fellowship. We are grateful for the use of NASA High-End Computing resources to conduct this work. This study was carried out using the SWMF and BATS-R-US tools developed at the University of Michigan's Center for Space Environment Modeling (CSEM). The modeling tools described in this publication are available online through the University of Michigan for download and are available for use at the Community Coordinated Modeling Center (CCMC). Model output and the code used to create the figures are available at the University of Michigan Deep Blue Data repository. The full 12-hr model output is found online (doi:10.7302/fwq2-ey41). This work only employs the last time slice at 12:00. The plotting code used is found online (doi:10.7302/7w13-kq27).

### References

- Cassak, P. A., & Shay, M. A. (2007). Scaling of asymmetric magnetic reconnection: General theory and collisional simulations. *Physics of Plasmas*, 14(10), 102114. <https://doi.org/10.1063/1.2795630>
- Chandler, M. O., & Moore, T. E. (2003). Observations of the geopause at the equatorial magnetopause: Density and temperature. *Geophysical Research Letters*, 30(16), 1869. <https://doi.org/10.1029/2003GL017611>
- Chapman, S., & Ferraro, V. C. A. (1931). A new theory of magnetic storms. *Terrestrial Magnetism and Atmospheric Electricity*, 36(2), 77–97. <https://doi.org/10.1029/TE036i002p00077>
- Chappell, C. R., Moore, T. E., & Waite, J. H. (1987). The ionosphere as a fully adequate source of plasma for the Earth's magnetosphere. *Journal of Geophysical Research*, 92(A6), 5896–5910. <https://doi.org/10.1029/JA092iA06p05896>
- De Zeeuw, D. L., Sazykin, S., Wolf, R. A., Gombosi, T. I., Ridley, A. J., & Tóth, G. (2004). Coupling of a global MHD code and an inner magnetospheric model: Initial results. *Journal of Geophysical Research*, 109, A12219. <https://doi.org/10.1029/2003JA010366>
- Dungey, J. W. (1961). Interplanetary magnetic field and the auroral zones. *Physical Review Letters*, 6, 47–48. <https://doi.org/10.1103/PhysRevLett.6.47>
- Glocer, A., Fok, M., Meng, X., Tóth, G., Buzulukova, N., Chen, S., & Lin, K. (2013). CRCM + BATS-R-US two-way coupling. *Journal of Geophysical Research: Space Physics*, 118, 1635–1650. <https://doi.org/10.1002/jgra.50221>
- Glocer, A., Tóth, G., Ma, Y., Gombosi, T., Zhang, J.-C., & Kistler, L. M. (2009). Multifluid Block-Adaptive-Tree Solar wind Roe-type Upwind Scheme: Magnetospheric composition and dynamics during geomagnetic storms—Initial results. *Journal of Geophysical Research*, 114, A12203. <https://doi.org/10.1029/2009JA014418>
- Haiducek, J. D., Welling, D. T., Ganushkina, N. Y., Morley, S. K., & Ozturk, D. S. (2017). SWMF global magnetosphere simulations of January 2005: Geomagnetic indices and cross-polar cap potential. *Space Weather*, 15, 1567–1587. <https://doi.org/10.1002/2017SW001695>
- Ilie, R., Ganushkina, N., Tóth, G., Dubyagin, S., & Liemohn, M. W. (2015b). Testing the magnetotail configuration based on observations of low-altitude isotropic boundaries during quiet times. *Journal of Geophysical Research: Space Physics*, 120, 10,557–10,573. <https://doi.org/10.1002/2015JA021858>
- Ilie, R., & Liemohn, M. W. (2016). The outflow of ionospheric nitrogen ions: A possible tracer for the altitude-dependent transport and energization processes of ionospheric plasma. *Journal of Geophysical Research: Space Physics*, 121, 9250–9255. <https://doi.org/10.1002/2015JA022162>
- Ilie, R., Liemohn, M. W., Kozyra, J., & Borovsky, J. (2010b). An investigation of the magnetosphere-ionosphere response to real and idealized co-rotating interaction region events through global magnetohydrodynamic simulations. *Proceedings of the Royal Society A: Mathematical, Physical and Engineering Sciences*, 466(2123), 3279–3303. <https://doi.org/10.1098/rspa.2010.0074>
- Ilie, R., Liemohn, M. W., & Ridley, A. (2010a). The effect of smoothed solar wind inputs on global modeling results. *Journal of Geophysical Research*, 115, A01213. <https://doi.org/10.1029/2009JA014443>
- Ilie, R., Liemohn, M. W., Tóth, G., Ganushkina, N. Y., & Daldorff, L. K. S. (2015a). Assessing the role of oxygen on ring current formation and evolution through numerical experiments. *Journal of Geophysical Research: Space Physics*, 120, 4656–4668. <https://doi.org/10.1002/2015JA021157>
- Ilie, R., Liemohn, M. W., Tóth, G., & Skoug, R. M. (2012). Kinetic model of the inner magnetosphere with arbitrary magnetic field. *Journal of Geophysical Research*, 117, A04208. <https://doi.org/10.1029/2011JA017189>
- Ilie, R., Skoug, R. M., Valek, P., Funsten, H. O., & Glocer, A. (2013). Global view of inner magnetosphere composition during storm time. *Journal of Geophysical Research: Space Physics*, 118, 7074–7084. <https://doi.org/10.1002/2012JA018468>
- Liemohn, M., Ganushkina, N. Y., De Zeeuw, D. L., Rastätter, L., Kuznetsova, M., Welling, D. T., et al. (2018). Real-time SWMF at CCMC: Assessing the Dst output from continuous operational simulations. *Space Weather*, 16, 1583–1603. <https://doi.org/10.1029/2018SW001953>
- Liemohn, M. W., & Welling, D. T. (2016). Ionospheric and Solar Wind Contributions to Magnetospheric Ion Density and Temperature throughout the Magnetotail. *Magnetosphere-ionosphere coupling in the solar system* (pp. 101–114), 8. Hoboken, NJ, USA: American Geophysical Union (AGU). <https://doi.org/10.1002/9781119066880.ch8>
- Meng, X., Tóth, G., Glocer, A., Fok, M.-C., & Gombosi, T. I. (2013). Pressure anisotropy in global magnetospheric simulations: Coupling with ring current models. *Journal of Geophysical Research: Space Physics*, 118, 5639–5658. <https://doi.org/10.1002/jgra.50539>
- Meng, X., Tóth, G., Liemohn, M. W., Gombosi, T. I., & Runov, A. (2012). Pressure anisotropy in global magnetospheric simulations: A magnetohydrodynamics model. *Journal of Geophysical Research*, 117, A08216. <https://doi.org/10.1029/2012JA017791>
- Moore, T. E., & Delcourt, D. C. (1995). The geopause. *Reviews of Geophysics*, 33(2), 175–209. <https://doi.org/10.1029/95RG00872>
- Moore, T. E., Peterson, W. K., Russell, C. T., Chandler, M. O., Collier, M. R., Collin, H. L., et al. (1999). Ionospheric mass ejection in response to a CME. *Geophysical Research Letters*, 26(15), 2339–2342. <https://doi.org/10.1029/1999GL000456>
- Pembroke, A., Toffoletto, F., Sazykin, S., Wiltberger, M., Lyon, J., Merkin, V., & Schmitt, P. (2012). Initial results from a dynamic coupled magnetosphere-ionosphere-ring current model. *Journal of Geophysical Research*, 117, A02211. <https://doi.org/10.1029/2011JA016979>
- Powell, K. G., Roe, P. L., Linde, T. J., Gombosi, T. I., & Zeeuw, D. L. D. (1999). A solution-adaptive upwind scheme for ideal magnetohydrodynamics. *Journal of Computational Physics*, 154(2), 284–309. <https://doi.org/10.1006/jcph.1999.6299>
- Pulkkinen, A., Kuznetsova, M., Ridley, A., Raeder, J., Vapirev, A., Weimer, D., et al. (2011). Geospace environment modeling 2008–2009 challenge: Ground magnetic field perturbations. *Space Weather*, 9, SO2004. <https://doi.org/10.1029/2010SW000600>
- Pulkkinen, A., Rastätter, L., Kuznetsova, M., Hesse, M., Ridley, A., Raeder, J., et al. (2010). Systematic evaluation of ground and geostationary magnetic field predictions generated by global magnetohydrodynamic models. *Journal of Geophysical Research*, 115, A03206. <https://doi.org/10.1029/2009JA014537>
- Pulkkinen, A., Rastätter, L., Kuznetsova, M., Singer, H., Balch, C., Weimer, D., et al. (2013). Community-wide validation of geospace model ground magnetic field perturbation predictions to support model transition to operations. *Space Weather*, 11, 369–385. <https://doi.org/10.1002/swe.20056>

- Rastätter, L., Kuznetsova, M. M., Glocher, A., Welling, D., Meng, X., Raeder, J., et al. (2013). Geospace environment modeling 2008-2009 challenge: Dst index. *Space Weather*, *11*, 187–205. <https://doi.org/10.1002/swe.20036>
- Rastätter, L., Kuznetsova, M. M., Vapirev, A., Ridley, A., Wiltberger, M., Pulkkinen, A., et al. (2011). Geospace environment modeling 2008-2009 challenge: Geosynchronous magnetic field. *Space Weather*, *9*, S04005. <https://doi.org/10.1029/2010SW000617>
- Ridley, A. J. (2007). Alfvén wings at Earth's magnetosphere under strong interplanetary magnetic fields. *Annales Geophysicae*, *25*(2), 533–542. <https://doi.org/10.5194/angeo-25-533-2007>
- Ridley, A. J., Gombosi, T. I., & De Zeeuw, D. L. (2004). Ionospheric control of the magnetosphere: Conductance. *Annales Geophysicae*, *22*(2), 567–584. <https://doi.org/10.5194/angeo-22-567-2004>
- Ridley, A. J., & Liemohn, M. W. (2002). A model-derived storm time asymmetric ring current driven electric field description. *Journal of Geophysical Research*, *107*(A8), SMP 2–1–SMP 2–12. <https://doi.org/10.1029/2001JA000051>
- Sharp, R. D., Lennartsson, W., Peterson, W. K., & Shelley, E. G. (1982). The origins of the plasma in the distant plasma sheet. *Journal of Geophysical Research*, *87*(A12), 10,420–10,424. <https://doi.org/10.1029/JA087iA12p10420>
- Shelley, E. G., Johnson, R. G., & Sharp, R. D. (1972). Satellite observations of energetic heavy ions during a geomagnetic storm. *Journal of Geophysical Research*, *77*(31), 6104–6110. <https://doi.org/10.1029/JA077i031p06104>
- Shim, J. S., Kuznetsova, M., Rastätter, L., Bilitza, D., Butala, M., Codrescu, M., et al. (2012). CEDAR electrodynamic thermosphere ionosphere (ETI) Challenge for systematic assessment of ionosphere/thermosphere models: Electron density, neutral density, NmF2, and hmF2 using space based observations. *Space Weather*, *10*, S10004. <https://doi.org/10.1029/2012SW000851>
- Siscoe, G. L., Erickson, G. M., Sonnerup, B. U. Ö., Maynard, N. C., Siebert, K. D., Weimer, D. R., & White, W. W. (2001). Global role of  $E_{\parallel}$  in magnetopause reconnection: An explicit demonstration. *Journal of Geophysical Research*, *106*(A7), 13,015–13,022. <https://doi.org/10.1029/2000JA000062>
- Song, P., De Zeeuw, D. L., Gombosi, T. I., Groth, C. P. T., & Powell, K. G. (1999). A numerical study of solar wind-magnetosphere interaction for northward interplanetary magnetic field. *Journal of Geophysical Research*, *104*(A12), 28,361–28,378. <https://doi.org/10.1029/1999JA900378>
- Tóth, G., De Zeeuw, D. L., Gombosi, T. I., Manchester, W. B., Ridley, A. J., Sokolov, I. V., & Roussev, I. I. (2007). Sun-to-thermosphere simulation of the 28-30 October 2003 storm with the Space Weather Modeling Framework. *Space Weather*, *5*, 06003. <https://doi.org/10.1029/2006SW000272>
- Tóth, G., van der Holst, B., Sokolov, I. V., Zeeuw, D. L. D., Gombosi, T. I., Fang, F., et al. (2012). Adaptive numerical algorithms in space weather modeling. *Journal of Computational Physics*, *231*(3), 870–903. <https://doi.org/10.1016/j.jcp.2011.02.006>, special Issue: Computational Plasma Physics.
- Welling, D. T., & Liemohn, M. W. (2014). Outflow in global magnetohydrodynamics as a function of a passive inner boundary source. *Journal of Geophysical Research: Space Physics*, *119*, 2691–2705. <https://doi.org/10.1002/2013JA019374>
- Welling, D. T., & Ridley, A. J. (2010). Exploring sources of magnetospheric plasma using multispecies MHD. *Journal of Geophysical Research*, *115*, A04201. <https://doi.org/10.1029/2009JA014596>
- Welling, D. T., Tóth, G., Jordanova, V. K., & Yu, Y. (2018). Integration of RAM-SCB into the space weather modeling framework. *Journal of Atmospheric and Solar-Terrestrial Physics*, *177*, 160–168. <https://doi.org/10.1016/j.jastp.2018.01.007>
- Wiltberger, M., Lotko, W., Lyon, J. G., Damiano, P., & Merkin, V. (2010). Influence of cusp O+ outflow on magnetotail dynamics in a multifluid MHD model of the magnetosphere. *Journal of Geophysical Research*, *115*, A00J05. <https://doi.org/10.1029/2010JA015579>
- Winglee, R. M. (1998). Multi-fluid simulations of the magnetosphere: The identification of the geopause and its variation with IMF. *Geophysical Research Letters*, *25*(24), 4441–4444. <https://doi.org/10.1029/1998GL900217>
- Winglee, R. (2000). Mapping of ionospheric outflows into the magnetosphere for varying imf conditions. *Journal of Atmospheric and Solar-Terrestrial Physics*, *62*(6), 527–540. [https://doi.org/10.1016/S1364-6826\(00\)00015-8](https://doi.org/10.1016/S1364-6826(00)00015-8)
- Winglee, R. M., Chua, D., Brittnacher, M., Parks, G. K., & Lu, G. (2002). Global impact of ionospheric outflows on the dynamics of the magnetosphere and cross-polar cap potential. *Journal of Geophysical Research*, *107*(A9), SMP 11–1–SMP 11–12. <https://doi.org/10.1029/2001JA000214>
- Xu, S., Liemohn, M. W., Dong, C., Mitchell, D. L., Bougher, S. W., & Ma, Y. (2016). Pressure and ion composition boundaries at Mars. *Journal of Geophysical Research: Space Physics*, *121*, 6417–6429. <https://doi.org/10.1002/2016JA022644>
- Young, D. T., Balsiger, H., & Geiss, J. (1982). Correlations of magnetospheric ion composition with geomagnetic and solar activity. *Journal of Geophysical Research*, *87*(A11), 9077–9096. <https://doi.org/10.1029/JA087iA11p09077>
- Yu, Y., & Ridley, A. J. (2009). Response of the magnetosphere-ionosphere system to a sudden southward turning of interplanetary magnetic field. *Journal of Geophysical Research*, *114*, A03216. <https://doi.org/10.1029/2008JA013292>
- Zhang, J., Liemohn, M. W., De Zeeuw, D. L., Borovsky, J. E., Ridley, A. J., Toth, G., et al. (2007). Understanding storm-time ring current development through data-model comparisons of a moderate storm. *Journal of Geophysical Research*, *112*, A04208. <https://doi.org/10.1029/2006JA011846>